

## LA-UR-19-28474

Approved for public release; distribution is unlimited.

Title: An examination of different representations of the electrostatic field and potential of an intense relativistic electron beam in a cylindrical conductor and their implications on foil focusing of an elliptical beam

Author(s): Schulze, Martin E.  
Schultz, Kimberly Ann  
Taccetti, Jose Martin

Intended for: Report

Issued: 2021-08-12 (rev.1)

---

**Disclaimer:**

Los Alamos National Laboratory, an affirmative action/equal opportunity employer, is operated by Triad National Security, LLC for the National Nuclear Security Administration of U.S. Department of Energy under contract 89233218CNA000001. By approving this article, the publisher recognizes that the U.S. Government retains nonexclusive, royalty-free license to publish or reproduce the published form of this contribution, or to allow others to do so, for U.S. Government purposes. Los Alamos National Laboratory requests that the publisher identify this article as work performed under the auspices of the U.S. Department of Energy. Los Alamos National Laboratory strongly supports academic freedom and a researcher's right to publish; as an institution, however, the Laboratory does not endorse the viewpoint of a publication or guarantee its technical correctness.

## An examination of different representations of the electrostatic field and potential of an intense relativistic electron beam in a cylindrical conductor and their implications on foil focusing of an elliptical beam

### Introduction

Knowledge of the electrostatic field and potential of an intense relativistic electron beam (IREB) in a cylindrical conductor is essential for understanding the transport of IREBs including the interaction of a grounded conducting foil with the beam. Different representations of the electrostatic field or potential exist in the literature [1-5]. The different representations are compared and an extension to foil focusing of elliptical beams is discussed.

The use of a thin foil with a pepper-pot pattern of holes to infer the emittance of an IREB is described by Schultz [6]. This concept relies on the fact that multiple Coulomb scattering (MCS) in a thin foil is much greater than the foil focusing. All of the beam is subject to foil focusing as long as the holes are smaller than the Debye length. The foil focusing experienced by the beams of interest for this effort is typically less than 10 mrad [7]. The MCS in the foil is typically over an order of magnitude higher for high Z foils. Thus, the beam that passes through the foil causes a small and essentially uniform background to the pepper-pot beamlets. The beams of interest have energies from 5 MeV to many 10s of MeV and currents of 500 A to a few kA.

### Review of Foil Focusing

Foil focusing of round uniform IREBs was first described by Adler [5] and the change in the radial angle,  $\delta\theta_r$ , is given as the ratio of the change in the radial momentum,  $\delta p_r$ , to the longitudinal momentum,  $p_z$ :

$$\delta\theta_r = \frac{\delta p_r}{p_z} = - \frac{16I}{I_A} \left( \frac{b}{r_b} \right) \sum_{n=1}^{\infty} \frac{J_1(\chi_n r_b | b)}{\chi_n^3 J_1^2(\chi_n)} J_1(\chi_n r | b) \quad (1)$$

Here,  $b$  is the radius of the cylindrical conductor,  $I$  is the beam current,  $r_b$  is the beam radius,  $I_A$  is the Alfvén current,  $J_n$  is the Bessel function of the first kind and  $\chi_n$  is the  $n$ th root of  $J_0$ . Fernsler et al. [1] derive the foil focusing of a few axisymmetric beam profiles including the round uniform beam.

A comparison of the foil focusing from (1) for different beam radii shows features that have been described by others. Figure 1 shows the calculated focusing angle for five different beam radii inside a 10 cm radius pipe. The calculation corresponds to a beam with 1650 A and 16.5 MeV as is the case throughout this report. These are the typical beam parameters in the DARHT II downstream transport. The foil focusing is seen to be stronger for smaller beam sizes on the foil which is expected due to the beam radius,  $r_b$ , in the denominator of (1). Figure 2 shows the same calculation with the initial beam size scaled to the beam radius. Another feature seen in these curves is the nonlinearity of the angular kick. The slope of the focusing kick decreases at larger beam radii compared to the

essentially linear kick in the center of the beam. This nonlinearity has been modeled as a first order spherical aberration by Ekdahl [7]. Figure 3 shows the deviation from a linear kick for two different beam radii with scaled beam radii as in Figure 2. This shows that the aberration is only slightly larger for larger ratios of the beam radius to the pipe radius. The difference in the aberration is about 5% for initial beam sizes that are a factor of five different.

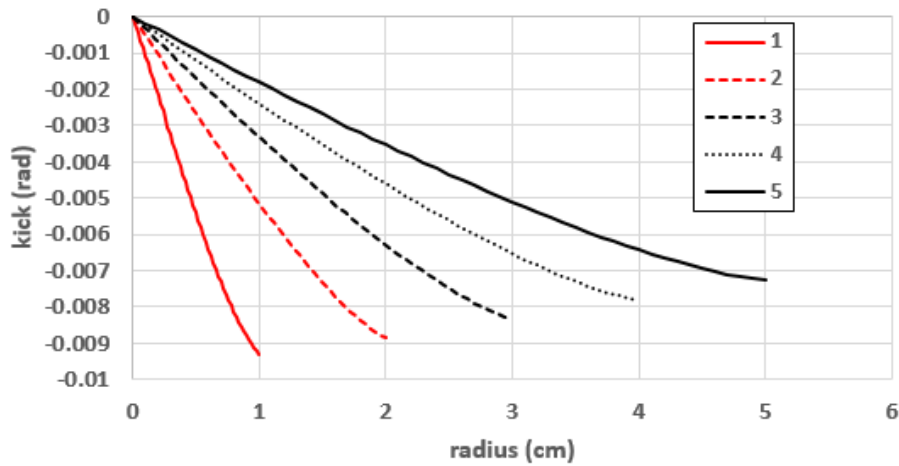


Figure 1: Focusing kick for uniform beams of different radii inside a grounded 10 cm radius beam pipe.

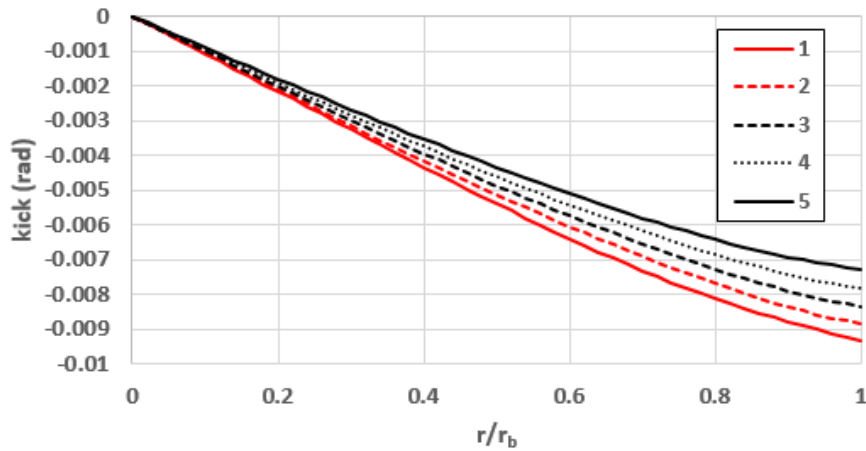


Figure 2: Focusing kick for uniform beams of different radii inside a grounded 10 cm radius beam pipe as in Figure 1. The focusing kick as a function of radius is scaled to the beam radius.

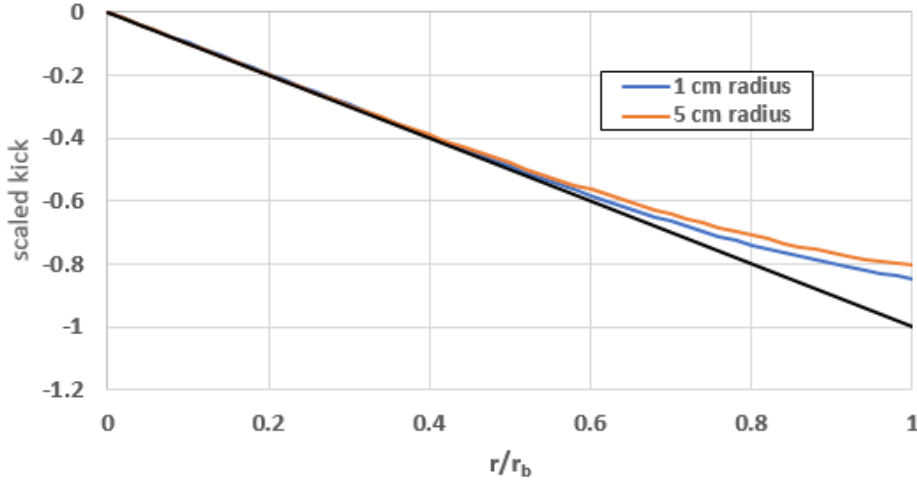


Figure 3: Focusing kick scaled to unity for a linear kick as a function of radius compared to the scaled kick for two different beam radii, 1.0 and 5 cm, in a 10 cm pipe. The ratio of the kick for the 1.0 and 5.0 cm beam radii compared to a linear kick is .847 and .804 respectively at  $r=r_b$ .

#### Derivation of foil focusing and extension to elliptical beams

The foil charge produces an electrostatic potential,  $\phi$ , satisfying

$$\nabla^2 \phi_f = 0, \quad (2)$$

with  $\phi_f$  equal to zero at  $z = \pm \infty$  and on the pipe,  $r = b$ . On the foil itself,

$$\phi_f(r) = -\phi_0(r) \quad (3)$$

where  $\phi_0(r)$  is the potential of the beam in the absence of the foil.

Fernsler et al. [1] give the following expression for the electrostatic potential,  $\phi(r,z)$ , as:

$$\phi(r,z) = \sum_{n=1}^{\infty} A_n e^{(-\chi_n |z|/b)} J_0(\chi_n r/b) \quad (4)$$

where,

$$A_n = \frac{8\pi}{c \chi_n^2 J_1^2(\chi_n)} \int_0^b dr r J_0(\chi_n r/b) j_b(r) \quad (5)$$

Here,  $j_b(r)$  is the beam current density and  $c$  is the speed of light. For a round beam of uniform density,

$$j_b(r) = \begin{cases} I/\pi b^2, & r \leq r_b \\ 0, & r > r_b \end{cases} \quad (6)$$

and

$$A_n = -8 \frac{I}{c} \frac{b}{r_b} \frac{J_1(\chi_n r_b/b)}{\chi_n^3 J_1^2(\chi_n)} \quad (7)$$

This is the result first described by Adler [5]. Calculations of foil focusing for different beam distributions including Gaussian and parabolic are also given by Fernsler [1].

The structure of (4) automatically satisfies the boundary conditions at  $z = \pm \infty$  and  $r=b$ . The repulsive space charge force of the beam is cancelled exactly on the foil and is partially cancelled as the

beam approaches and leaves the region of the foil. The change in transverse momentum as the beam passes through the foil is given by (8).

$$\delta p_r = - \int_{-\infty}^{\infty} dz \frac{e}{v_z} \frac{\partial \phi_f}{\partial r} = \frac{2e}{c} \sum_{n=1}^{\infty} A_n J_1 (\chi_n r | b) \quad (8)$$

The integral over  $z$  produces a factor of  $2b/\chi_n$  and the derivative produces a factor of  $\chi_n/b$  resulting in a factor of 2. This results in the angular kick given in (1).

Furman [2] and Lund [3] calculate the electric field of an elliptical beam distribution inside a conducting beam tube using a combination of the method of images and the calculus of complex variables. The electric field is expressed as the sum of the direct field in the absence of a conducting cylinder and the image field imposed by the beam on the vacuum chamber. The direct field is readily calculated from the potential of a uniform elliptical beam distribution,  $\phi(x,y)$  for a beam centered in the circular vacuum chamber.

$$\phi(x,y) = -2\lambda \left[ \frac{x^2}{(r_x+r_y)r_x} + \frac{y^2}{(r_x+r_y)r_y} \right] + const \quad (9)$$

Here  $r_x$  and  $r_y$  and the semi major and minor axes of the ellipse and  $\lambda$  is the charge per unit length. Appendix A provides a discussion of the direct and image fields for an elliptical beam and shows that image fields contribute less than 1% to the overall field for beams in which the major axis of the ellipse is less than  $\frac{1}{2}$  the beam pipe radius. For a round beam centered in the beam pipe there are no image fields.

We now compare the results of Adler/NRL and Lund by calculating the electric field of a round beam at  $z=0$ . From (9), we have for Lund:

$$E_r(r) = \frac{2I}{cr_b^2} r \quad (10)$$

From (5), we have for Adler/NRL:

$$E_r(r) = \sum_{n=1}^{\infty} \frac{\chi_n}{b} A_n J_1 (\chi_n r | b) \quad (11)$$

Figure 4 compares the electric fields calculated with (10 and (11) for a beam of 2 cm radius in a 5 cm radius pipe. The field calculated with (10) is perfectly linear as expected while the result from (11) shows some nonlinearity especially at larger radii. The nonlinearity appears to be due to the number of terms that are summed. Figure 4 uses the first 20 terms of (11). Figure 5 shows the sensitivity to the number of terms,  $n$ , for the same beam and pipe size. As  $n$  is increased from 7 to 20, the linearity increases and for sufficiently large  $n$  the result will be identical to that of (11). Compared to (1) there is an additional factor of  $\chi_n$  in the denominator that decreases the contribution from larger  $n$ . Based on this comparison, the two solutions appear identical and the closed form solution of (10) is much more straight forward and easier to use. These equations are only applicable for a round beam that is centered in the beam pipe.

The non-linearity in the focusing force results from the size of the beam relative to the pipe radius. The focusing force is due to the longitudinal dependence of the radial field as the beam is accelerated towards the foil and decelerated leaving the foil. Near the center of the foil the equipotential lines are parallel to the foil whereas at larger radii the equipotential lines are rounded due to the finite size of the beam. At larger radii, the radial electric field is lower than that extrapolated from the linear dependence at smaller radii leading to the nonlinearities and reduction in the focusing

strength. This can be seen in Figures 6a and 6b which show the equipotential lines for a 2.5 and 4.0 cm radius disks in a grounded 5 cm radius tube, respectively. Although the equipotential lines along the surface of the disk look very similar, the greater compression of the field lines at the edge of the 4.0 cm disk leads to more curvature and reduced radial electric field. This results in greater nonlinearity as shown in Figure 3.

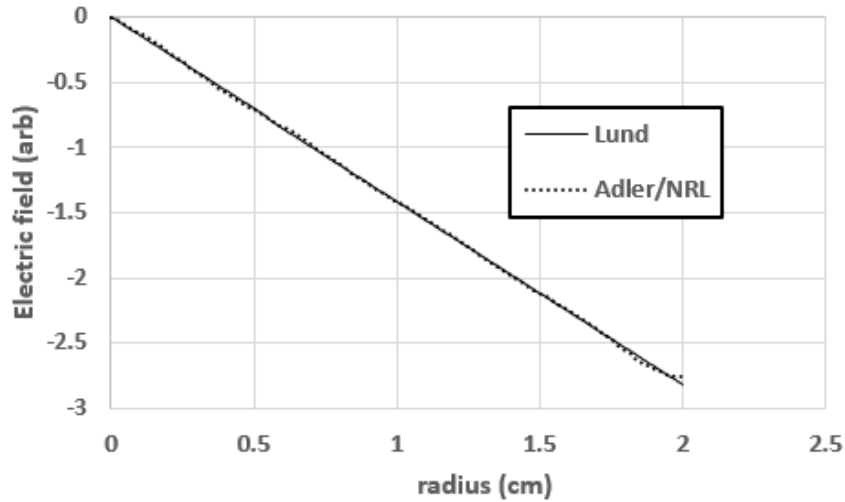


Figure 4: Calculated electric fields from (13) and (14) for a beam of 2 cm radius in a 5 cm radius pipe.

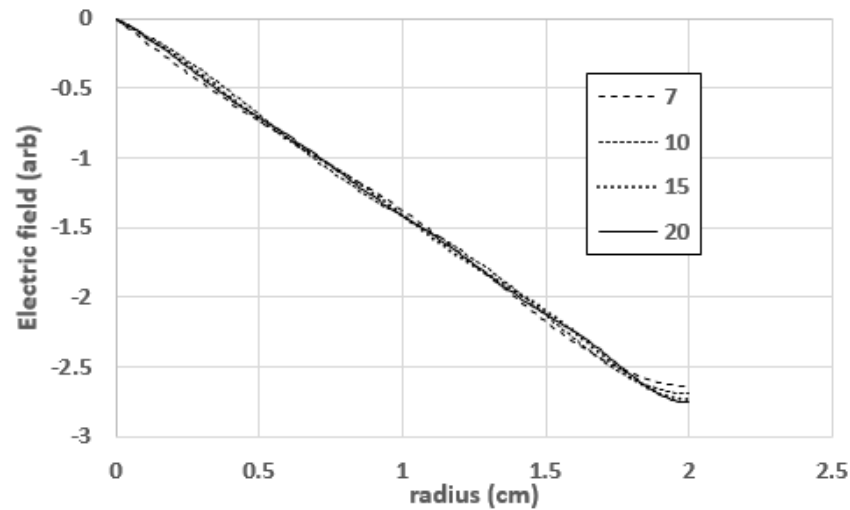


Figure 5: Calculated electric fields from (14) for a beam of 2 cm radius in a 5 cm radius pipe for different amount of terms in the summation.

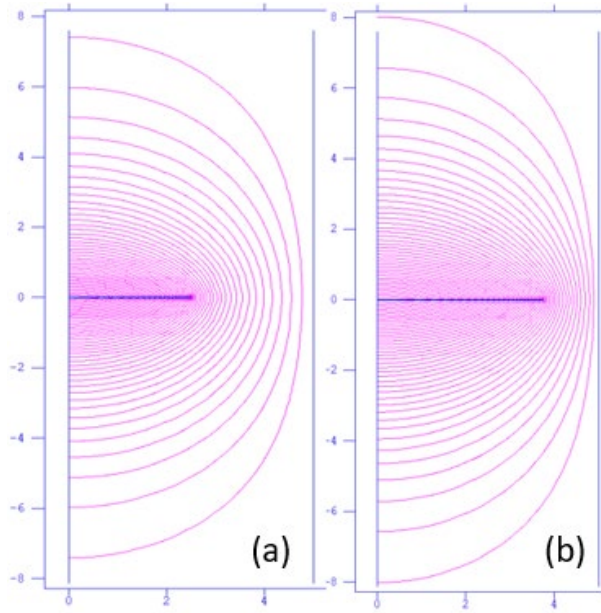


Figure 6: POISSON simulation of a charged circular disk in a grounded beam tube. Figures a and b show the respective equipotential lines for a 2.5 and 4.0 cm radius disks in a beam tube of 5.0 cm radius.

#### Longitudinal dependence of the radial electric field of a charged disc in a grounded beam tube

The radial kick shown in (8) is the integral of the radial electric field in the longitudinal plane. The longitudinal dependence of the potential given in (4) satisfies the boundary conditions at  $z = \pm \infty$  but shows no direct sensitivity to the beam size. One would expect the longitudinal field to be sensitive to the beam size and pipe radius.

The solution for the on axis potential of a uniformly charged disk (charge density  $\sigma$ ) in free space given in (12) shows no exponential fall off.

$$V(z) = 2\pi\sigma[\sqrt{r_b^2 + z^2} - |z|] \quad (12)$$

However, the presence of the grounded beam pipe will cause the fall off with  $z$  to increase.

A POISSON simulation was performed to better understand the potential and field of a charged disk in a grounded beam tube. A charged disk of 2 cm radius centered inside a 5 cm radius beam tube (200 cm long) was modeled and compared to Adler's/NRL's result as shown in Figure 7. As seen in Figure 7 the field drops off more rapidly in the POISSON simulation. The discrepancy seen in Figure 7 does not appear to be due to the number of terms in the Bessel expansion. There is a strong sensitivity to the foil thickness and mesh size. The longitudinal dependence of the potential in the absence of a beam tube is also shown. This implies that for larger beam pipe radii, the radial electric field of a disk will decrease more slowly with distance. This will lead to smaller non-linearities also.

Appendix B provides a more complete description of efforts to simulate the field of a charged disc in a grounded beam tube using both POISSON and ANSYS for circular and elliptical beams respectively. These simulations provide similar results that do not agree with the Adler/NRL closed form solution. The simulation results show much smaller non-linear effects as described in Appendix B.



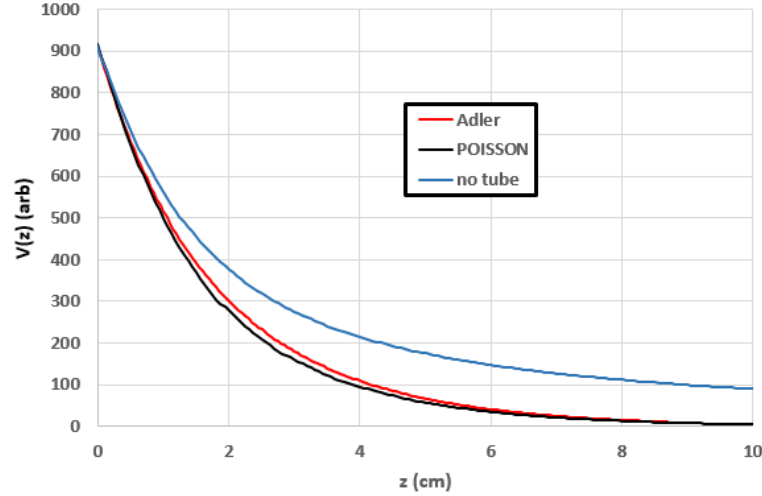


Figure 7: Comparison of the longitudinal dependence of the on axis potential for a 2 cm radius beam in a 5 cm radius pipe.

Equation 13 shows the longitudinal and radial dependence of the radial electric field.

$$E_r(r, z) = \sum_{n=1}^{\infty} \frac{\chi_n}{b} A_n J_1(\chi_n r | b) e^{(-\chi_n |z| | b)} \quad (13)$$

Figure 8 shows a calculation of the radial electric field given by (13) as a function of radius for a 5 cm radius disk in a 10 cm tube for different longitudinal distances from the foil. Figure 9 shows a similar calculation of the radial electric field for a 2.5 cm radius disk in a 5 cm tube. Each of these figures corresponds to the same aspect ratio of the beam radius to the pipe radius. Comparison of these two figures illustrates many features of foil focusing. The horizontal axis of both figures extends out to the beam radius. At the beam radius, the electric field on the foil ( $z=0$ ) for the 2.5 cm beam radius (Figure 8) is twice that for the 5.0 cm beam in a 10 cm tube due to the factor of  $r_b$  in the denominator as given in (7). Comparing Figures 8 and 9 shows that the electric field decreases more rapidly with the distance from the foil for the smaller beam size.

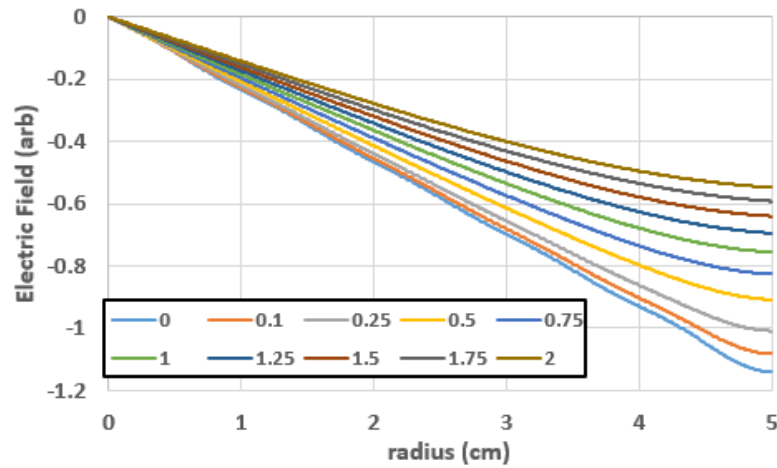


Figure 8: Radial dependence of the electric field for different distances from the foil in cm for a 5 cm radius disk in a 10 cm radius tube for different distances from the foil as identified in the legend.

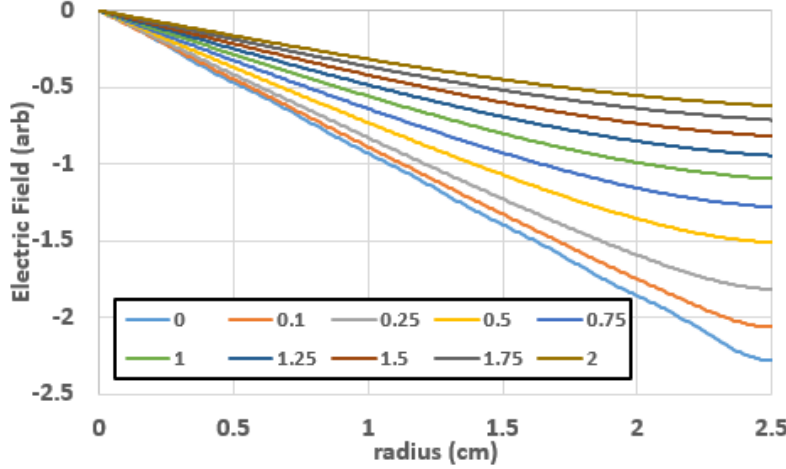


Figure 9: Radial dependence of the electric field for different distances from the foil in cm for a 2.5 cm radius disk in a 5 cm radius tube for different distances from the foil as identified in the legend.

One would also expect that for the same aspect ratio (distance from the foil scaled by the ratio of the beam sizes), the shape of the radial field should be identical. This is shown in Figure 10 for four different geometries. The radial electric field is plotted as a function of radius at a distance from the foil that is 10% of the beam radius. The four curves appear to be identical. The field for the 2.5 cm beam in a 5 cm pipe is not scaled. The field for the 5 cm beam in a 10 cm pipe is scaled by a factor of two. The fields for the 2 cm beam in a 4 and 5 cm pipe are both scaled by a factor of 0.8. Since each of these curves corresponds to the same beam current, the curves scale with the beam radius as seen in (7). Conversely, the electric field at a distance from the foil scaled by the beam radius scales inversely with the beam radius. Figure 11 shows the scaled radial electric field for the same four geometries at a distances equal to the beam radius. The scaling factors are the same as in Figure 10. Here we see that the scaled field for the geometry with the different aspect ratio of the beam radius to pipe radius does not scale by the same factor. This is not seen in Figure 9 due to the very small distance from the foil ( $z=0.1r_b$ ).

Figure 12 shows that the scaling depends on the ratio of the beam radius to the pipe radius for the case  $r_b/b=0.4$ . The larger pipe radius results in a slower longitudinal falloff or radial field as seen in Figure 6. Thus, for constant  $r_b/b$ , the longitudinal and radial dependence of the radial electric field scales with beam radius as given in (14).

$$E_{(r_b=r_1)}(r/r_1, z) = \frac{r_2}{r_1} E_{(r_b=r_2)}(r/r_2, zr_2/r_1) \quad (14)$$

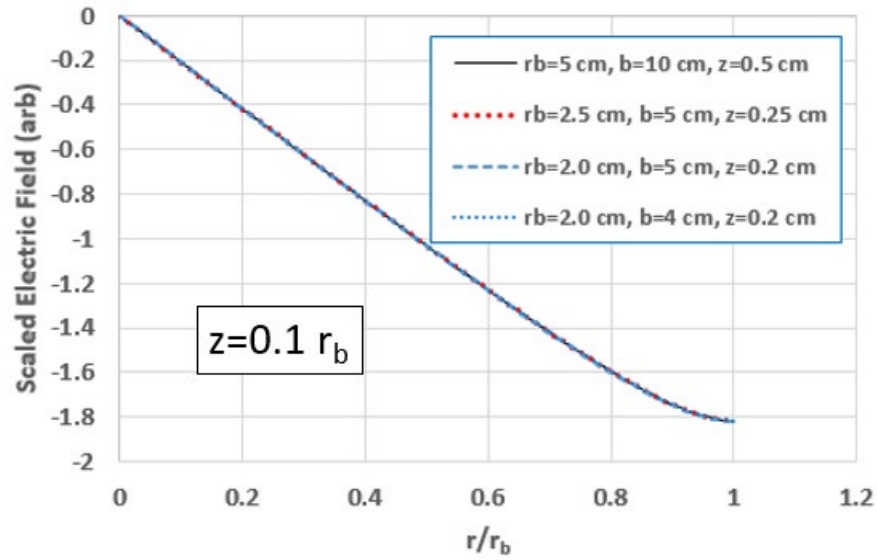


Figure 10: Plot of scaled radial electric field at a distance scaled by the beam radius ( $z=0.1 r_b$ ) for four different geometries as described in the text.

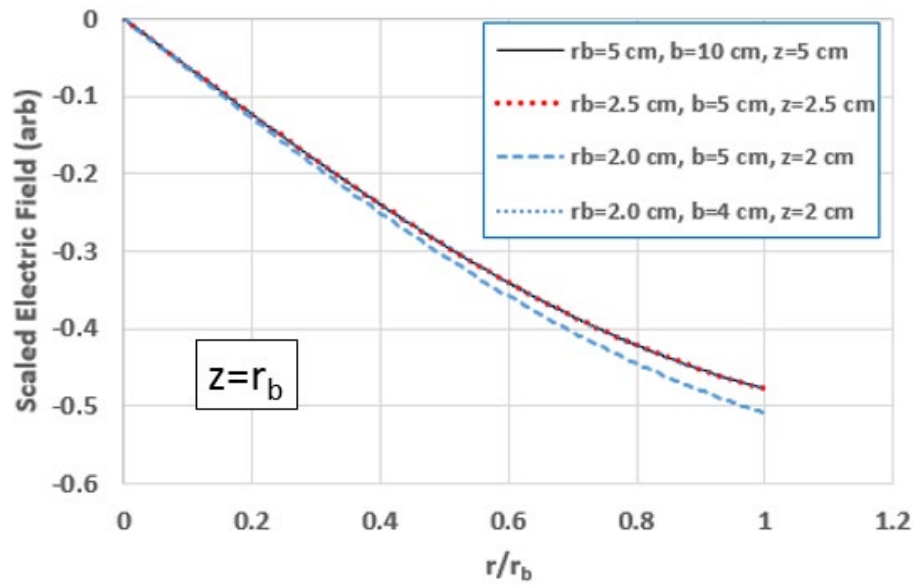


Figure 11: Plot of scaled radial electric field at a distance scaled by the beam radius ( $z=r_b$ ) for four different geometries as described in the text.

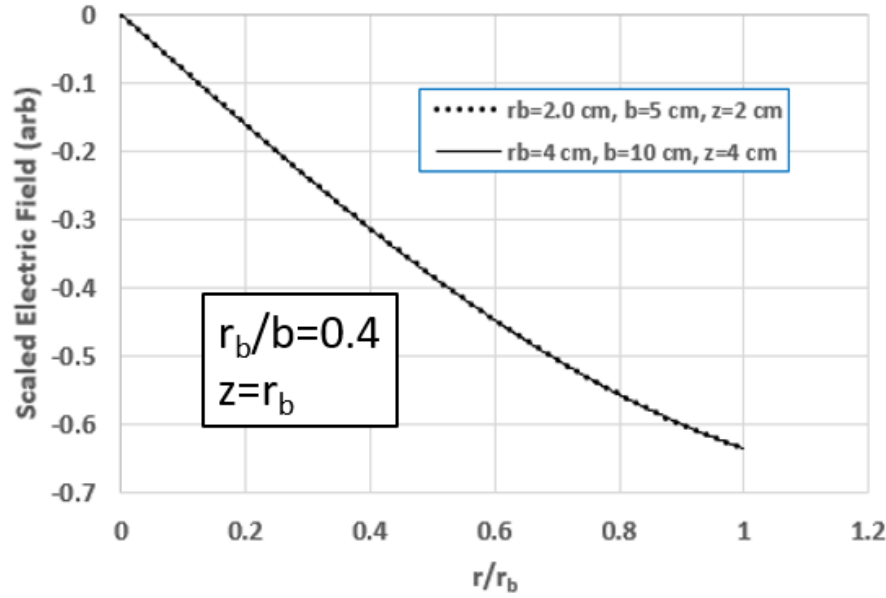


Figure 12: Plot of scaled radial electric field at a distance scaled by the beam radius ( $z=r_b$ ) for two different geometries as described in the text.

We will now examine the longitudinal shape of the radial electric field for different beam and pipe geometries. Figure 13 shows the radial electric field as a function of the distance from the foil for different discrete radii out to the foil/beam radius for a 5 cm beam in a 10 cm pipe. Figure 14 shows the radial electric field as a function of the distance from the foil for different discrete radii out to the foil/beam radius for a 2.5 cm beam in a 5 cm pipe. The plots clearly show the radial electric field decreases much more rapidly as the radius approaches the beam radius. The curves correspond to eleven values of the radius that represent the same fraction of the beam radius. Plotting the fields out to a distance equal to the beam radius in Figures 13 and 14 results in two identical plots except for a factor of two in the vertical scale. This is consistent with (14). Figure 15 shows the radial electric field for two cases shown in Figures 13 and 14 corresponding to values of  $r/r_b$  of .8 and 1.0.

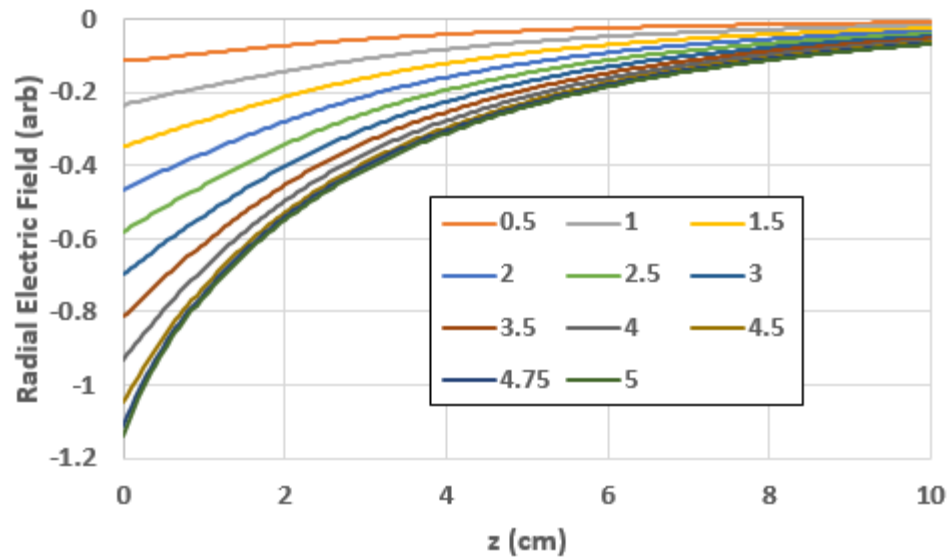


Figure 13: Radial electric field as a function of the distance from the foil for different discrete radii out to the foil/beam radius for a 5 cm beam in a 10 cm pipe.

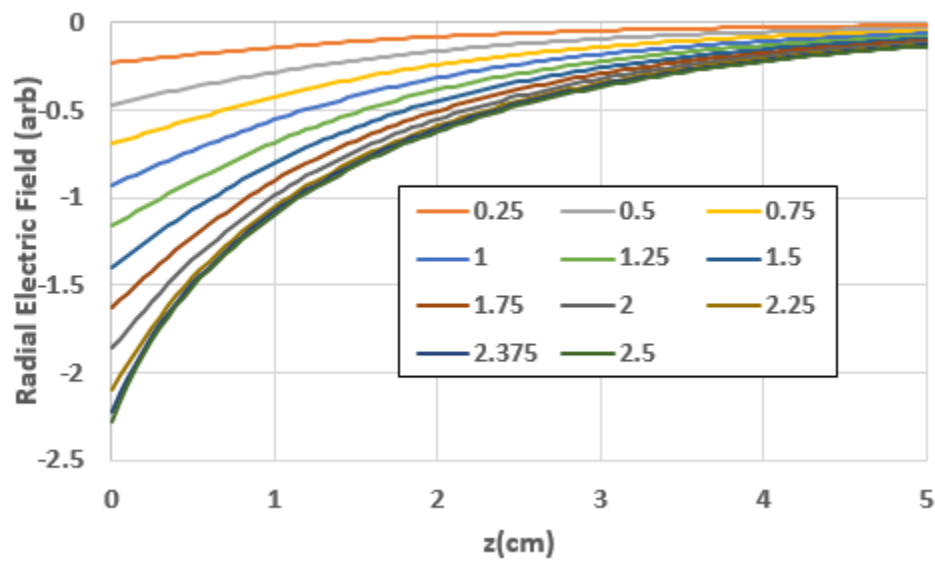


Figure 14: Radial electric field as a function of the distance from the foil for different discrete radii out to the foil/beam radius for a 2.5 cm beam in a 5 cm pipe.

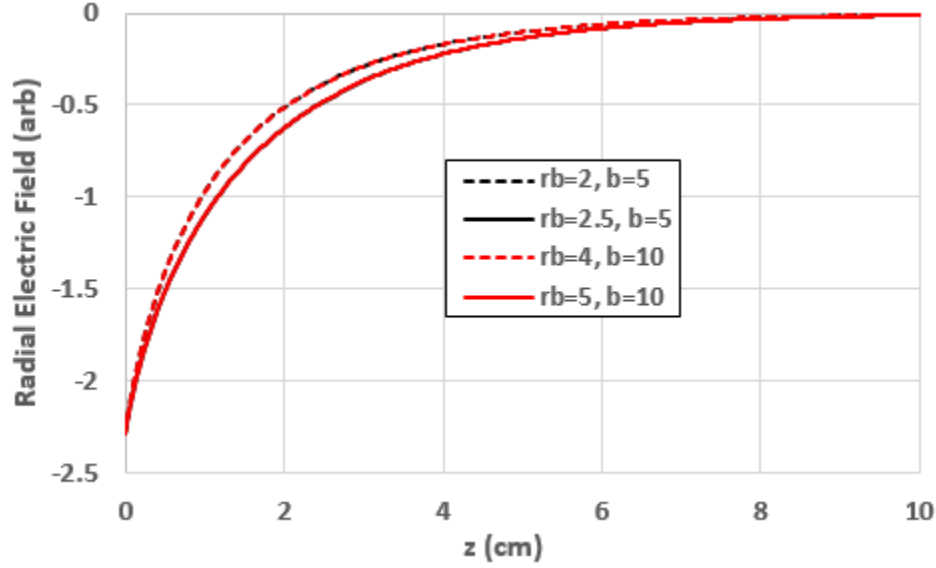


Figure 15: Overlay of the scaled radial electric field as a function of the distance from the foil for values of  $r/r_b$  of 0.8 and 1.0.

### Estimated foil focusing of elliptical beams

Although a closed form solution does not exist, foil focusing of elliptical beams will have many of the characteristics described above. Based on the characteristics of foil focusing of round beams described above we make the case for an empirical description of foil focusing of elliptical beams. As shown in (8), the change in the transverse momentum is given by the longitudinal integral of the radial electric field. We have shown that on the foil the radial electric field is linear for round beams. As shown in Appendix A, the radial electric field on the foil for an elliptical beam is linear to better than 1% for beams whose semi major axis is less than  $\frac{1}{2}$  of the pipe radius. The deviation from a linear kick with radius is governed by the radial fall-off of the radial electric field with distance from the foil. This will also be the case for elliptical beams. Thus, it is the difference in the deviation from a linear kick with radius between a round and an elliptical beam that is in question.

As shown in Figure 3, the focusing kick is essentially linear for particles within  $\frac{1}{2}$  of the beam radius. This should also be the case for elliptical beams with  $r_y \geq .5r_x$  where  $r_x$  and  $r_y$  are the semi-major and semi-minor axes of the ellipse as depicted in Figure 16. Figure 3 also shows that the variation from a linear kick varies by only 5.2% at the beam radius for  $0.1 < r_b/b < 0.5$ . This implies that the use of (1) with  $r_b = r_b(\theta)$  for elliptical beams with  $r_y \geq .5r_x$  will be accurate to a few percent. This is shown in (15).

$$\delta\theta_r = \frac{\delta p_r}{p_z} = - \frac{16I}{I_A} \left( \frac{b}{r_b(\theta)} \right) \sum_{n=1}^{\infty} \frac{J_1(\chi_n r_b(\theta) |b)}{\chi_n^3 J_1^2(\chi_n)} J_1(\chi_n r |b) \quad (15)$$

Here,

$$r_b(\theta) = \frac{r_y}{(1 - (e \cos(\theta))^2)^{1/2}} \quad (16)$$

where the ellipticity,  $e$ , is defined in (17).

$$e = \left( 1 - \left( r_y/r_x \right)^2 \right)^{1/2} \quad (17)$$

Figures 17a and 18a show the foil focusing kick for two different ellipses with a semi-major axis of 2.0 cm and semi-minor axes of 1.0 and 1.5 cm respectively. Figures 17b and 18b show the foil focusing kick for the same two ellipses as a function of the scaled radius,  $r/r(\theta)$ . The pipe radius is 10 cm in these calculations. Figures 17 and 18 show that the initial slope is inversely proportional to  $r(\theta)$  as can be expected from the electric field (see (A1)). Figures 17b and 18b show that the variation of the focusing angle over the circumference of the ellipse is very small with a 5% and 2.7% variation for the ellipses with semi-minor axes of 1.0 and 1.5 cm respectively. This supports the approximation given in (15) for ellipses in which the semi-major and semi-minor axes are less than a factor of two different or  $r_y \geq 0.5r_x$ .

Errors in this approximation will arise from the change in the longitudinal fall off of the radial electric field due to the shape of the ellipse. In the region of the semi-minor axis, the longitudinal field is likely to fall off more gradually due to the larger effective width of the field on the foil. This would result in reduced nonlinearity. The converse would be expected in the region of the semi major axis. Based on the above discussion, these errors are not expected to be very large. Appendix C provides a sample analysis of a uniform elliptical beam distribution.

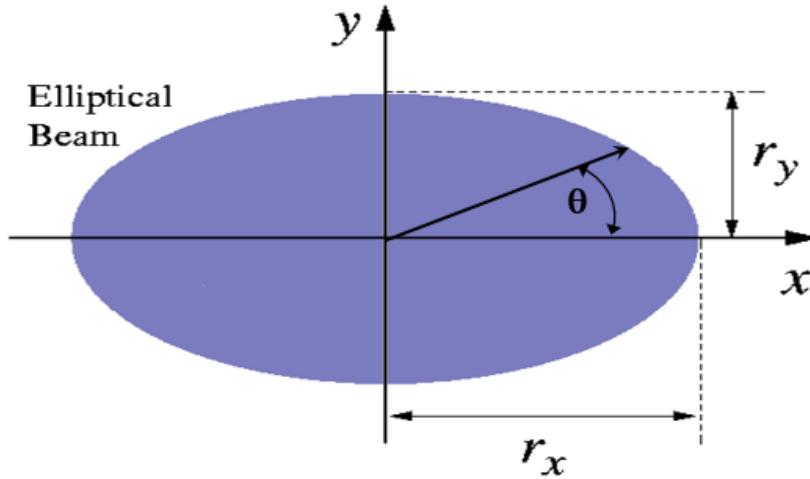


Figure 16: Schematic illustration of elliptical beam for semi-major axis given by  $r_x$  and semi-minor axis given by  $r_y$ .

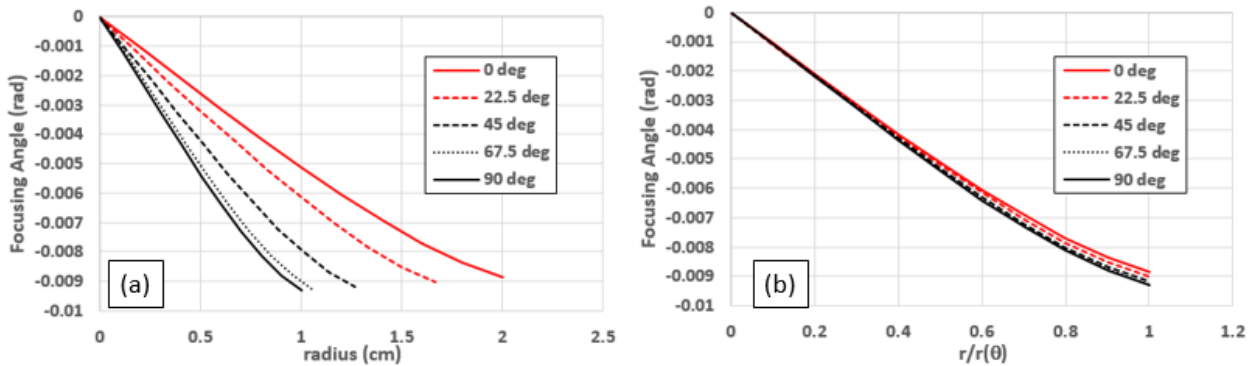


Figure 17: The foil focusing angle as a function of the distance from the ellipse center for different angles is shown in Figure 17a on the left. Figure 17b shows the same kick for the scaled radius. The semi-major and semi-minor axes are 2.0 and 1.0 cm respectively. The semi-major (0 deg) and semi-minor (90 deg) axes are 2.0 and 1.0 cm respectively.

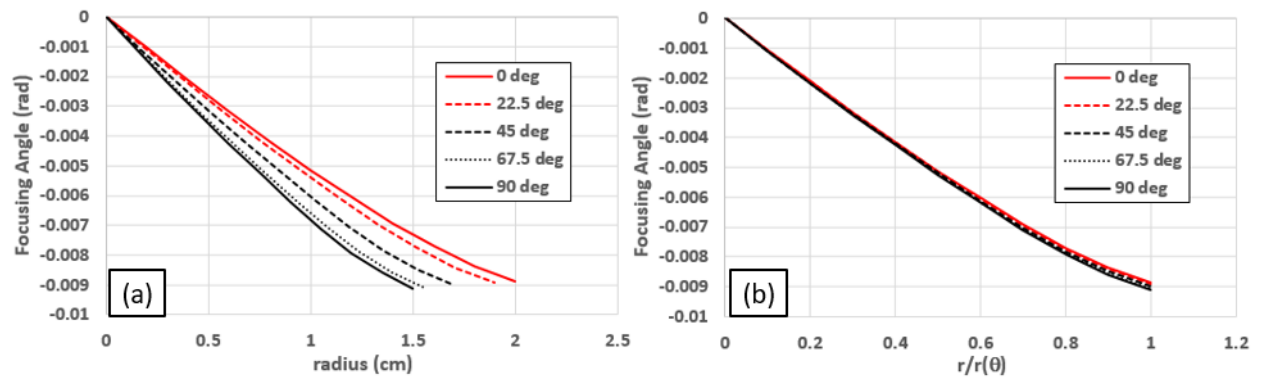


Figure 18: The foil focusing angle as a function of the distance from the ellipse center for different angles is shown in Figure 18a on the left. Figure 18b shows the same kick for the scaled radius. The semi-major and semi-minor axes are 2.0 and 1.5 cm respectively. The semi-major (0 deg) and semi-minor (90 deg) axes are 2.0 and 1.5 cm respectively.

## Conclusion

We have shown that the adaptation of the foil focusing of round beams to elliptical beams should not result in significant errors in the calculation of the emittance of elliptical beams with aspect ratios of less than two. This is because the differences in the nonlinearities at the beam edge are very small.

## References

- [1] R.F. Fernsler, R.F. Hubbard and S.P. Slinker, "Foil focusing of electron beams", *Journal of Applied Physics* **68**, 5985 (1990).
- [2] M.A. Furman, "Electric field of a 2D elliptical charge distribution inside a cylindrical conductor", *PRSTAB*, **10**, 081001 (2007).
- [3] S.M. Lund, USPAS, 2017, "Transverse Centroid and Envelope Descriptions of Beam Evolution", [https://people.nsl.msui.edu/~lund/uspas/bpisc\\_2017/lec\\_set\\_07/tce.pdf](https://people.nsl.msui.edu/~lund/uspas/bpisc_2017/lec_set_07/tce.pdf).
- [4] E. Regenstreif, "Potential and field created by an elliptical beam inside an infinite cylindrical vacuum chamber of circular cross section", *CERN/PS/DL 77-37*.
- [5] R.J. Adler, "Image Field Focusing of Intense Ultra-relativistic Electron Beams in Vacuum", *Particle Accelerators*, **12**, 39 (1982).
- [6] K.A. Schultz et al., "Novel Emittance Measurement Combining Foil Focusing and Pepper-Pot Techniques", *North American Particle Acc. Conf., NAPAC2019, Lansing, MI, USA*, pp 961-964.
- [7] C.A. Ekdahl, "Foil focusing of relativistic electron beams", *LA-UR-17-29832*.



## Appendix A

The direct field is readily calculated from the potential of a uniform elliptical distribution,  $\phi(x,y)$ . As given in (9), from which we determine the direct electric fields,  $E_x^d(x)$  and  $E_y^d(y)$  as given in (A1).

$$E_x^d(x) = -\frac{\partial\phi}{\partial x} = 4\lambda \frac{x}{(r_x+r_y)r_x}, \quad E_y^d(y) = -\frac{\partial\phi}{\partial y} = 4\lambda \frac{y}{(r_x+r_y)r_y} \quad (\text{A1})$$

Equation (A1) is valid only within the beam envelope. The image fields due to a beam pipe of radius  $b$  are given by Lund [3] as a complex number such that,

$$E^{i*} = E_x^i - iE_y^i = \sum_{n=2,4,\dots}^{\infty} c_n z^{n-1} \quad \text{where } z = x + iy \quad (\text{A2})$$

$$c_n = \frac{\lambda n!}{2^{(n+1)}(n/2+1)!(n/2)!} \left( \frac{r_x^2 - r_y^2}{b^4} \right)^{n/2} \quad (\text{A3})$$

From (A2) and (A3), we calculated the first two terms of the image field expansion. Equations A4 and A5 give the two terms ( $n=2$  and  $n=4$ ) in the expansion of the indirect field.

$$E_x^i(x) = \frac{\lambda}{2} \frac{r_x^2 - r_y^2}{b^4} x, \quad E_y^i(y) = \frac{\lambda}{2} \frac{r_x^2 - r_y^2}{b^4} y \quad (\text{A4})$$

$$E_x^i(x, y) = \frac{\lambda}{4} \left( \frac{r_x^2 - r_y^2}{b^4} \right)^2 (x^3 + 3x^2y), \quad E_y^i(x, y) = -\frac{\lambda}{4} \left( \frac{r_x^2 - r_y^2}{b^4} \right)^2 (y^3 + 3xy^2) \quad (\text{A5})$$

The contribution of the image field is very small and vanishes for a round beam. As seen in (A4) and (A5), the leading order corrections for an on axis beam very small compared to the direct beam. The image fields are very small for small beam ellipticities and larger pipe radii. Figures A1 and A2 show the effect of the image field corrections for an electric field,  $E_x$ , of an elliptical beam with major and minor axes of 4 and 1 cm in pipe radii of 10 and 7.5 cm respectively. The image field corrections are seen to be very small in both cases. The contribution of the  $n=2$  term is less than 1% for beams in which the major axis is less than  $\frac{1}{2}$  of the pipe radius. Similarly, the contribution of the  $n=4$  term is less than 0.01% for beams in which the major axis is less than  $\frac{1}{2}$  of the pipe radius. Figures A3 and A4 show the fractional contribution of the image fields for  $n=2$  as a function of the major axis,  $r_x$  for two different pipe radii. This demonstrates that the image fields can be neglected in foil focusing of elliptical beams as long as the ellipticity is small ( $r_x/r_y < 2.5$ ) and the ratio of the major axis to the pipe radius is less than 0.5.

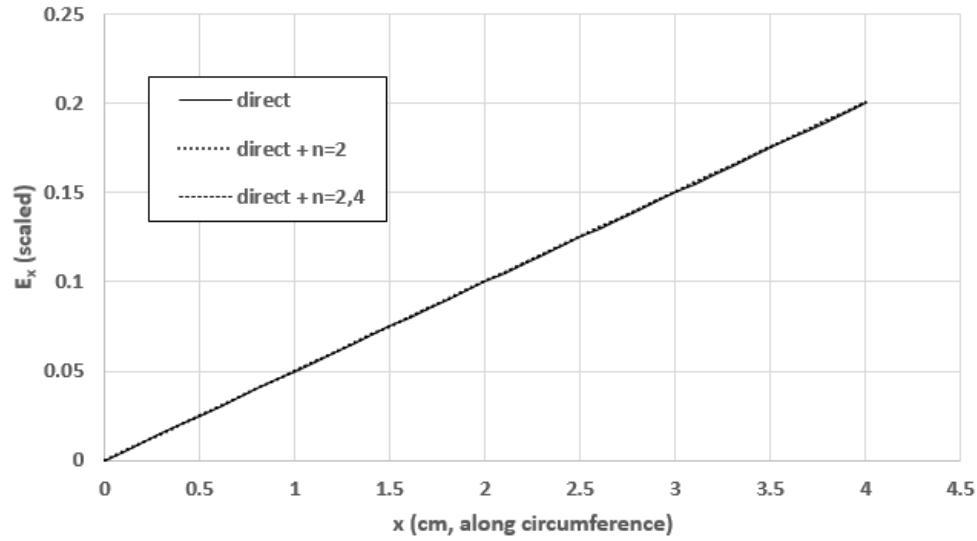


Figure A1: Plot of the direct field,  $E_x^d$  along the circumference along with the first two terms of the indirect correction due to the beam pipe. The major (horizontal) and minor (vertical) axes of the ellipse are 4 and 1 cm respectively and the pipe radius is 10 cm.

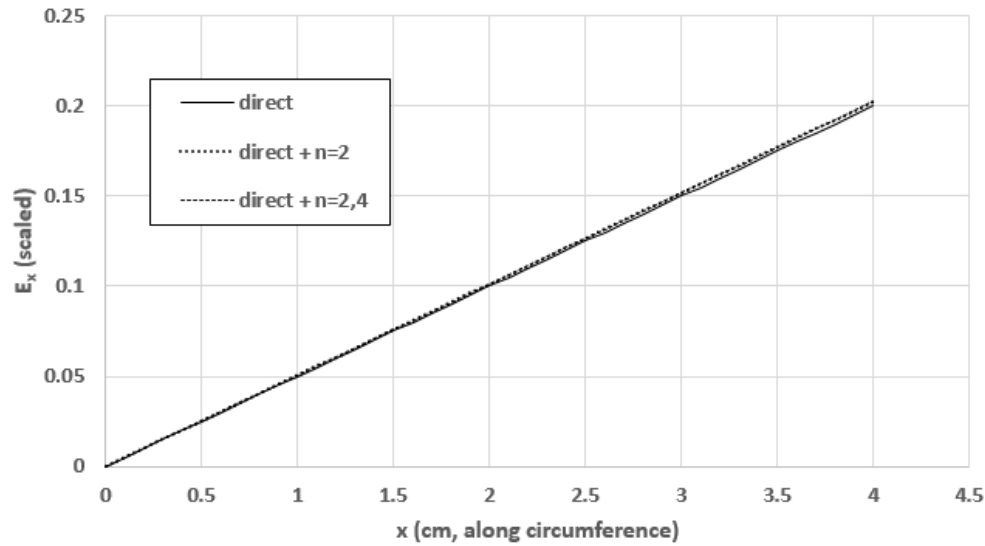


Figure A2: Plot of the direct field,  $E_x^d$  along the circumference along with the first two terms of the indirect correction due to the beam pipe. The major (horizontal) and minor (vertical) axes of the ellipse are 4 and 1 cm respectively and the pipe radius is 7.5 cm.

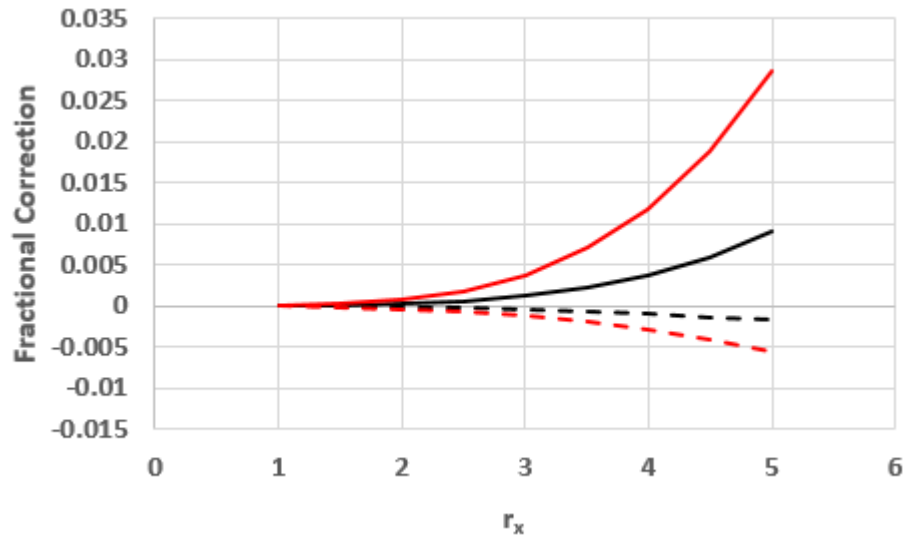


Figure A3: Fractional contribution of the image field to the direct field as a function of the major axis of the ellipse for a minor axis of 1 cm. The black and red curves correspond to a 10 and 7.5 cm pipe respectively. The solid curves are for the horizontal field,  $E_x$ , and the dashed curves are for the vertical field,  $E_y$ .

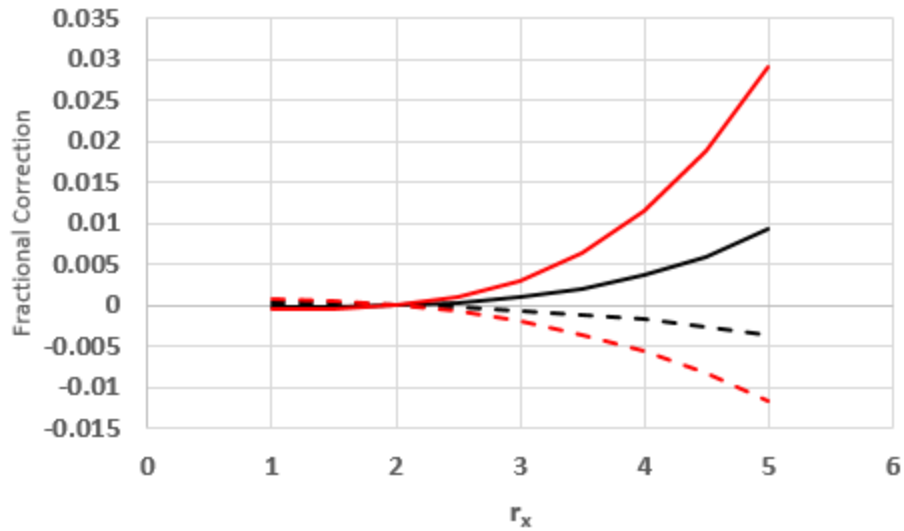


Figure A4: Fractional contribution of the image field to the direct field as a function of the major axis of the ellipse for a minor axis of 2 cm. The black and red curves correspond to a 10 and 7.5 cm pipe respectively. The solid curves are for the horizontal field,  $E_x$ , and the dashed curves are for the vertical field,  $E_y$ .

## Appendix B

In this appendix, simulation results from POISSON and ANSYS are compared with the closed form solution of Adler/NRL. The radial electric field from Adler/NRL (Eq. 13) is plotted in Figure B1 as a function of  $z$  for different beam radii. The spot size was 2 cm radius in a 5 cm pipe. The focusing angle is proportional to the integral of these curves and it is clear that the ratio of the focusing strength to the beam radius is decreasing as the radius increases. Figure B2 shows the same radial electric field calculated using POISSON. The major difference in these two figures is the radial electric field at large radii. The POISSON and ANSYS simulations used a foil of finite thickness resulting in field enhancement at the edge. While the case of a infinitely thin uniformly charged disk would introduce more enhancement, the grounded foil extending to the pipe wall is a different situation that is not readily modeled by POISSON or ANSYS. The simulation of a charged disk resulted in a stronger focusing kick as shown in Figure B3. Figure B4 shows a similar result comparing the focusing kick from (15) with the results from an ANSYS simulation for an elliptical disk with a semi-major and semi-minor radii of 2.0 and 1.0 cm respectively. Note that the focusing kick from the POISSON and ANSYS simulations are integrals of  $E_r(z)$  each scaled by the same amount.

These comparisons indicate that the POISSON and ANSYS simulations do not give accurate calculations of the longitudinal dependence of the radial electric field. This is presumed to be due to the fact that these codes do not accurately model a charge distribution of a grounded foil. The codes require one to enter a very high permittivity for a charge distribution of finite radius. This leads to field enhancements at the edge of the foil resulting in very strong sensitivity to the mesh size and foil thickness.

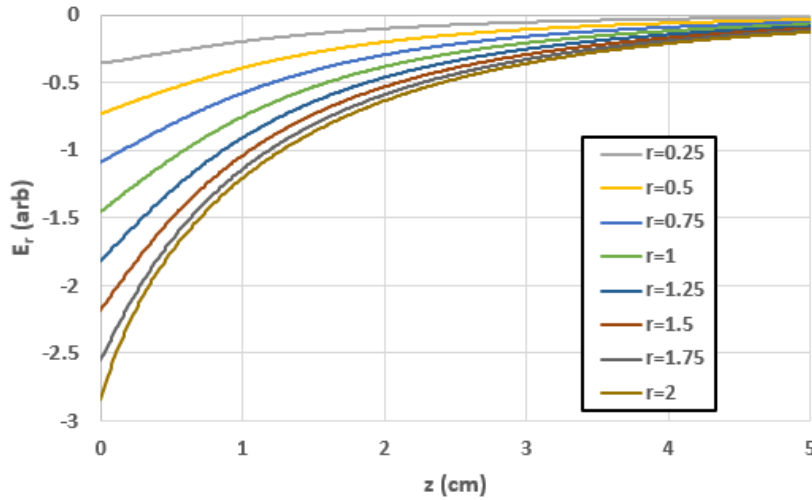


Figure B1: Radial electric field as a function of  $z$  for a 2 cm radius disc in a 5 cm radius tube from Adler/NRL (Eq. 13). The radial electric field is shown for a different beam radii.

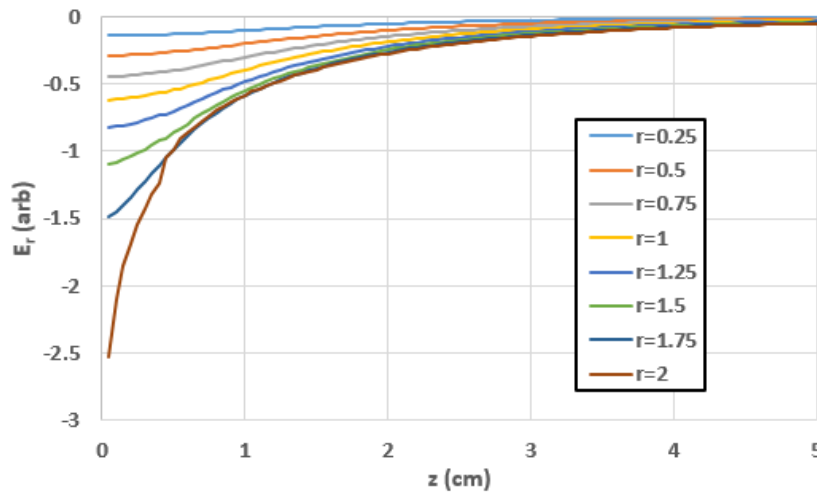


Figure B2: Radial electric field as a function of  $z$  for a 2 cm radius disc in a 5 cm radius tube as calculated using POISSON. The radial electric field is shown for a different beam radii.

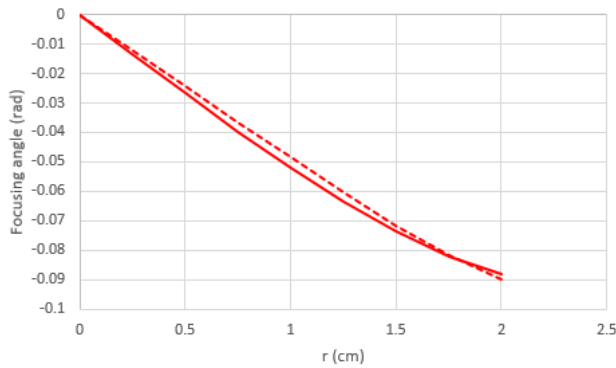


Figure B3: Comparison of the focusing kick calculated from the Adler/NRL (solid red line) and the POISSON simulation (dashed red line).

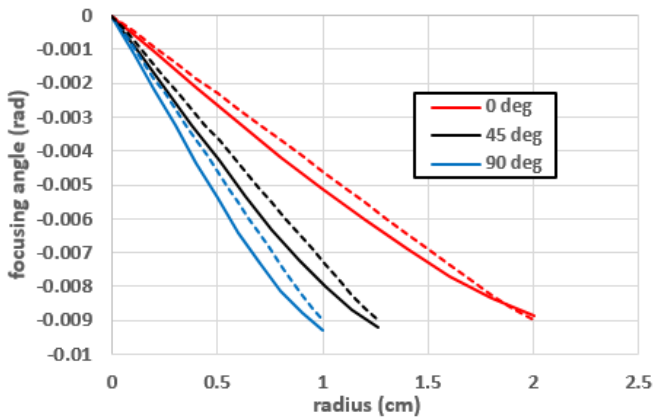


Figure B4: Comparison of the focusing kick calculated from (15) (solid lines) and the ANSYS simulation (dashed lines) for an elliptical disc with semi-major and semi-minor radii of 2.0 and 1.0 cm respectively. Results are presented for three angles as indicated by the legend.

## Appendix C

The pepperpot screen is located 1.574 m upstream of the OTR imaging station (ISC). The pepperpot image is shown in Figure C1 from Axis 2 shot 35092. The pepperpot screen was made of 0.010" Mo with 1.5 mm holes spaced 5 mm apart on center. From this we can determine the initial beam position at the pepperpot and estimate the ellipse size and orientation. This is presented in Figure C2. The ellipse has a semi-major axis of 21 mm and a semi-minor axis of 14.25 and is rotated clockwise by 14 deg. Also shown in Figure C2 are the pepperpot locations at ISC.

One of the key assumptions is that the beam distribution is uniform. Figure C3 shows the beam distribution in the absence of the pepperpot grid with line-outs. Figure C4 shows the horizontal and vertical distributions within these line-outs. As seen in Figure C4, the distributions are very close to uniform. Figure C5 shows the beam current is about 1.6 kA and that there is a small amount of beam scraping.

We apply Eq 15 to determine the foil focusing of each beamlet. The beam radius,  $r$ , of each beamlet is determined from the initial position on the pepperpot screen and the beam edge radius,  $r_b(\theta)$ , is determined from the angle of each beamlet and the rotated ellipse shown in Figure C2. The difference between this foil focusing angle and the angle calculated from the red and blue dots in Figure C2 determines the angle of the beamlet at the pepperpot screen in the absence of foil focusing. This allows us to estimate the phase ellipse in each plane as shown in Figures C6 and C7 respectively for the horizontal and vertical planes. The 95% normalized emittances calculated from the area of these ellipses is  $599 \pi(\text{mm-mrad})$  and  $932 \pi(\text{mm-mrad})$  for the horizontal and vertical planes respectively. The phase ellipses show some evidence of aberrations and do not consider the area of each beamlet. It is also noteworthy that the vertical emittance is significantly larger than the horizontal emittance.

One observation with regard to Figure C2 is that there are some beamlets at the edge of the ellipse which implies that the beam is somewhat larger. Figure C8 shows the same beamlets with the semi-major and minor axes 10% larger. The same calculation for this case yields very similar phase ellipses with 95% normalized emittances of  $559 \pi(\text{mm-mrad})$  and  $998 \pi(\text{mm-mrad})$  respectively in the horizontal and vertical planes. The differences between these numbers is indicative of the systematic errors in the calculation. The large difference between the horizontal and vertical planes is attributed to both beam scraping and higher order aberration in the Collins quadrupoles that distort the large vertical beam and not the smaller horizontal beam.

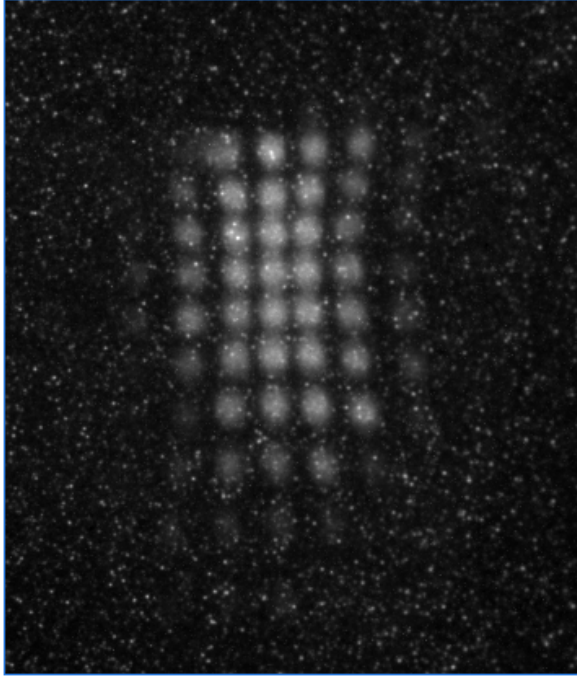


Figure C1: Pepperpot image for shot 35092

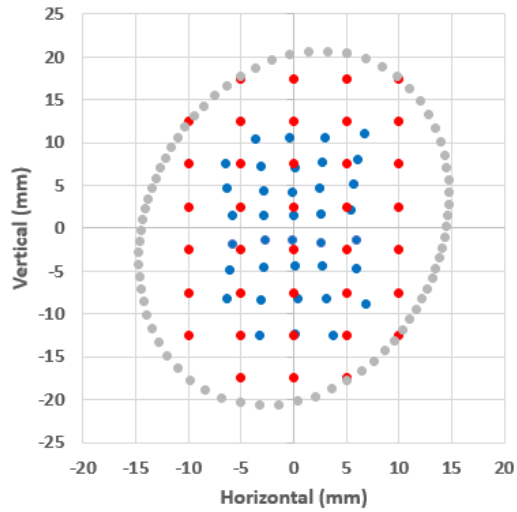


Figure C2: Location of initial beam position as given by the pepperpot image in Figure C1 in red. The measured location of the pepperpot image at ISC in blue. The ellipse given by the grey dots represents the estimated image at the pepperpot based on the red dots.

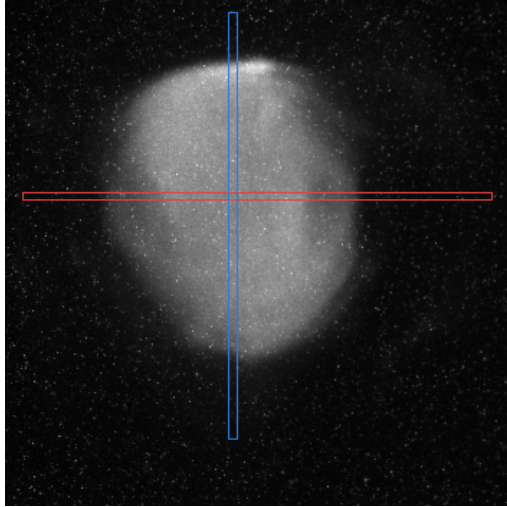


Figure C3: Beam spot at ISC in the absence of the pepperpot grid showing horizontal and vertical lineouts in red and blue respectively

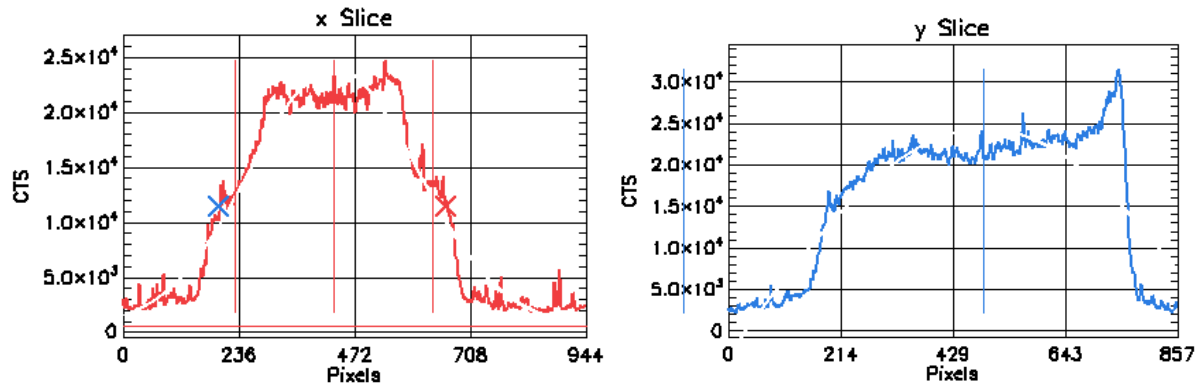


Figure C4: The horizontal (left) and vertical (right) beam distributions within the line-outs

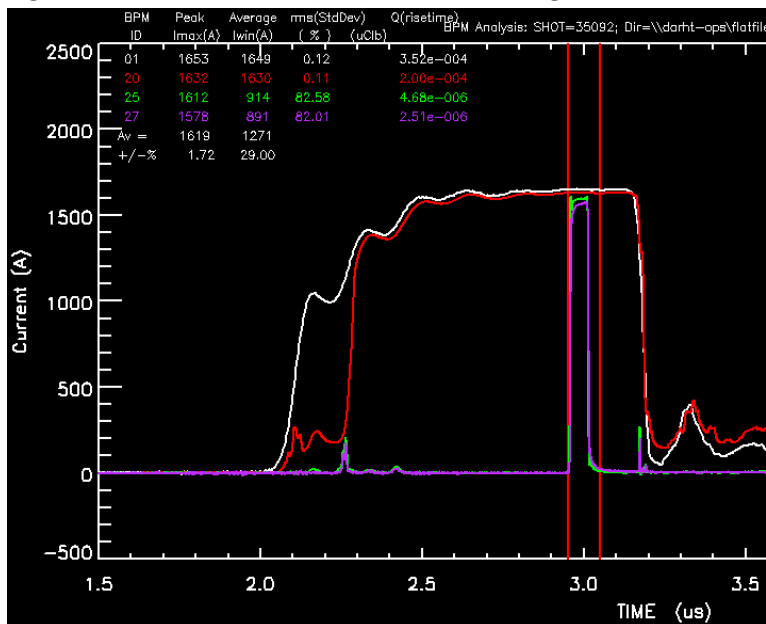


Figure C5: Beam current of the kicked beam pulse showing a small amount of beam scraping in the kicked pulse



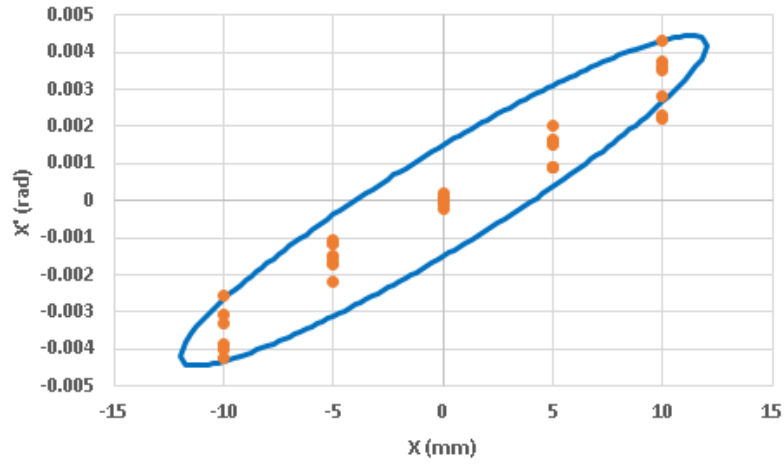


Figure C6: Horizontal phase ellipse of the beam at the pepperpot screen corresponding to Figure C2

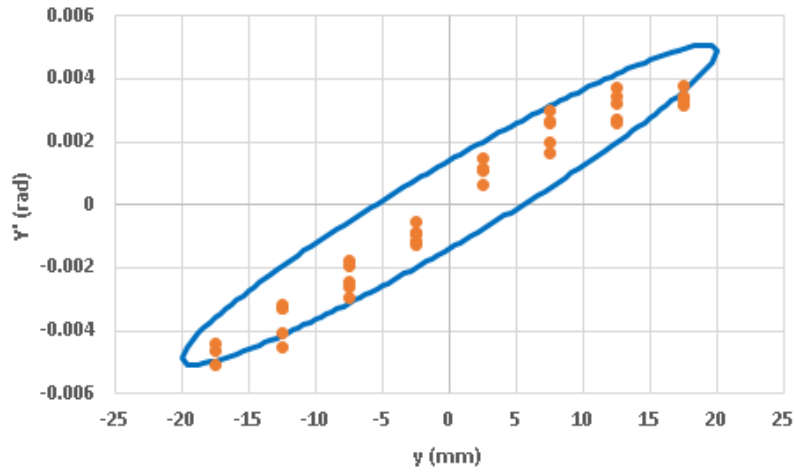


Figure C6: Vertical phase ellipse of the beam at the pepperpot screen corresponding to Figure C2

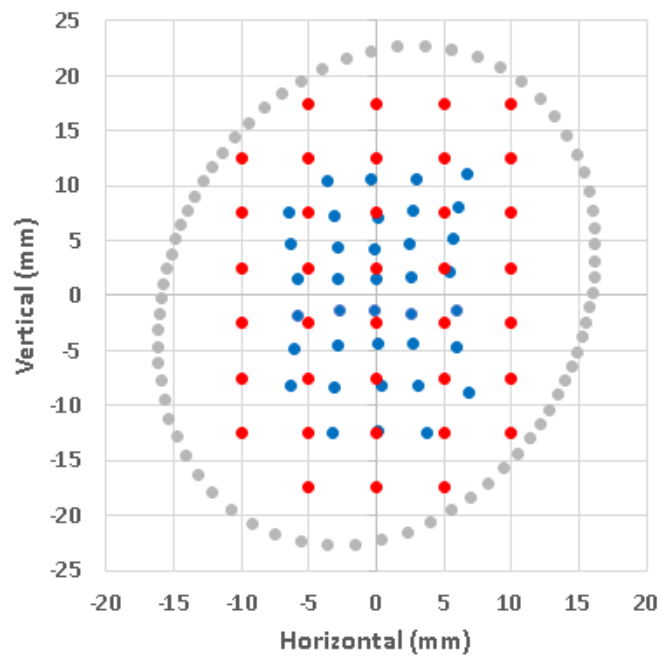


Figure C8: Beamlet distribution in a larger beam ellipse.